

**MSC-E Technical Note 8/2001**

**June 2001**

**HEMISPHERIC MODEL OF AIRBORNE POLLUTANT  
TRANSPORT**

Oleg Travnikov

**Meteorological Synthesizing Centre - East**

Kedrova str. 8-1, 117292 Moscow, Russia

Tel.: +7 095 124 47 58

Fax: +7 095 125 24 09

E-mail: [msce@msceast.org](mailto:msce@msceast.org)

[www.msceast.org](http://www.msceast.org)



## Contents

<b>Summary</b>	5
<b>1. Introduction</b>	7
<b>2. Model description</b>	9
2.1 Model domain	9
2.2 Basic equations	10
2.3 Horizontal advection	11
2.4 Vertical advection	14
2.5 Vertical diffusion	15
2.6 Removal processes	16
<b>3. Meteorological and emissions data</b>	17
<b>4. Model verification</b>	18
4.1 Comparison with regional MSCE-HM model	17
4.2 Comparison with measurements	22
<b>5. Preliminary results of lead airborne transport modelling</b>	23
5.1 Air concentration and deposition fields	23
5.2 Deposition from the continents and regions	24
5.3 Vertical distribution of lead concentration in air	26
<b>6. Conclusions</b>	28
<b>Acknowledgements</b>	29
<b>References</b>	30
<b>Annex A.</b> Bott advection scheme in spherical co-ordinates	31



## *Summary*

Assessment of the long-range airborne transport of volatile contaminants as mercury and some persistent organic pollutants (POPs) requires hemispheric or even global consideration. The main reason of that is a long atmospheric residence time estimated at months or even years, and making possible the airborne transport of these pollutants practically over the whole globe. The work on the development of a hemispheric airborne pollutant transport model has been carried out in Meteorological Synthesizing Centre – East of EMEP (EMEP/MSC-E) for last two years. The model is related to the family of three-dimensional Eulerian-type models and operates in the spherical (geographical) coordinates. The computational domain covers the whole Northern Hemisphere with spatial resolution  $2.5^{\circ} \times 2.5^{\circ}$ . At the first stage of the model development the atmospheric transport module has been elaborated. It is based on the flux-form Bott advection scheme adapted to the spherical coordinates. The elaborated model has been thoughtfully tested and verified. Testing of the advection scheme has shown that the model can adequately simulate pollutant transport in the atmosphere and does not produce significant numerical errors and distortions. The complete hemispheric model has been compared with the regional MSCE-HM model. The comparison has demonstrated that modelling results obtained by the hemispheric model are in satisfactory agreement with those of the regional one within European region. The hemispheric modelling results were also compared with the available measurements. It has been shown that the observed and modelled values agree within a factor of two. Preliminary results of lead airborne transport over the Northern Hemisphere have been obtained and discussed. Further stages of the model development are to include adaptation of the model to the airborne transport of mercury and selected POPs (lindane, PCB etc.) as well as elaboration of the chemical and deposition modules for these pollutants on the base of the multi-compartment approach to the environmental pollution assessment. It is also planned to extend the model to the global level with finer resolution ( $1^{\circ} \times 1^{\circ}$ ).



## 1. Introduction

Global character of the air pollution by some contaminants requires appropriate approaches to the assessment of their dispersion in the atmosphere. There are at least several reasons for the hemispheric or global consideration of the atmospheric pollutant dispersion. Firstly, volatile contaminants such as mercury and some POPs (HCB, lindane etc.) emitted to the atmosphere have essentially global atmospheric residence time estimated at months or even years and can be airborne transported practically over the whole globe [Lindqvist and Rodhe, 1985; Vulykh and Putilina, 2000]. Moreover, after the deposition to the Earth's surface these pollutants can be re-emitted to the atmosphere from areas far from traditionally considered industrial regions. Besides, the problem of contamination of such remote regions as the Arctic can be considered only at the hemispheric or global level.

Nowadays, this problem becomes topical for the environmental community. A considerable progress in collaborative efforts of different countries to prevent global pollution of the environment has been recently achieved within the framework of UNEP. As a result the Stockholm Convention on Persistent Organic Pollutants has been signed by 92 countries (UNEP/POPs/CONF/2, 2001). Besides, the Bureau of the Executive Body for the UN/ECE Convention on Long-Range Transboundary Air Pollution (CLRTAP) also invited UNEP to initiate assessment of mercury as a global pollutant and to consider the future joint activity. Evaluation of the atmospheric pollution at the hemispheric/global level was started under the CLRTAP in 2000 and was specified in "Strategy for EMEP 2000-2009" (EB.AIR/GE.1/2000/5).

The work on the hemispheric model elaboration is carried out in Meteorological Synthesizing Centre – East of EMEP (EMEP/MSCE) in accordance with its work-plan for 2001 (ECE/EB.AIR/71, annex IV) and with support of the Arctic Monitoring and Assessment Programme (AMAP). Current technical note describes development of the hemispheric model and its verification. The model relates to the family of three-dimensional Eulerian-type models and operates in the spherical (geographical) co-ordinates. The first stage of the model development was mostly devoted to elaboration of the atmospheric transport module. Description of the model is presented in Section 2 of the technical note. This section also contains the most important testing results of the numerical advection scheme utilized in the model. Section 3 is devoted to brief description of the meteorological data system elaborated for the model support and emission data used for the model verification. In spite of the fact that the hemispheric model is mostly developed to evaluate the atmospheric dispersion of volatile pollutants such as mercury and some POPs, the model transport and deposition characteristics have been verified on the base of lead as a pollutant simpler for interpretation. The hemispheric model verification is described in Section 4. Results of the hemispheric modelling have been compared with those of the operational MSCE-HM model and with the available measurement data. Section 5 contains preliminary results of lead hemispheric

transport modelling obtained by the model elaborated. Spatial distribution fields of mean annual lead concentration and total annual deposition have been calculated. Deposition fields from different continents and regions have been also evaluated in order to assess the main pathways of lead transport in the atmosphere. Vertical profiles of lead concentration in the atmosphere have been computed as well. The results presented have discussible character and are used illustrate the model ability to calculate hemispheric airborne transport. The main conclusions are summarized in Section 6. Finally, Annex A presents detailed description of the model advection scheme.

Further stages of the model development are to include:

- ! adaptation of the model to the airborne transport of mercury and selected POPs (lindane, PCB etc.) ;
- ! development and integration of the multi-compartment approach to the environmental pollution assessment;
- ! the model extension to the global level with finer resolution ( $1^{\circ}\times 1^{\circ}$ ).

## 2. Model description

The model of long-range pollutant transport over the Northern Hemisphere developed in MSC-E is related to the family of fully three-dimensional Eulerian-type models. This section is devoted to the description of the model structure, transport scheme, and deposition processes. The most important testing results of the employed numerical advection scheme are also adduced.

### 2.1. Model domain

The hemispheric model operates in geographical coordinates with the spatial resolution  $2.5^\circ \times 2.5^\circ$ . The computational domain covers the whole Northern Hemisphere and has an open boundary stretching along the Equator. Horizontal grid structure of the model domain is shown in Figure 2.1. To avoid a singularity at the pole point peculiar to the spherical coordinates the grid has a special circular mesh including the North Pole.

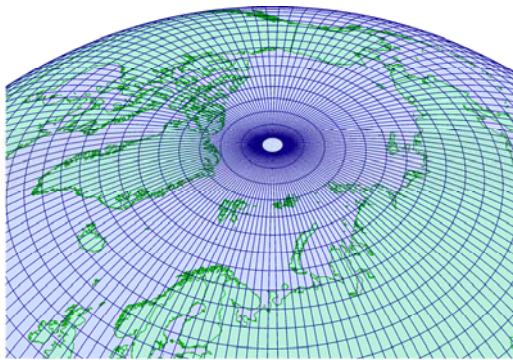


**Figure 2.1.** Horizontal grid structure of the model domain. Geographical coordinates with  $2.5^\circ \times 2.5^\circ$  resolution and the pole grid cell

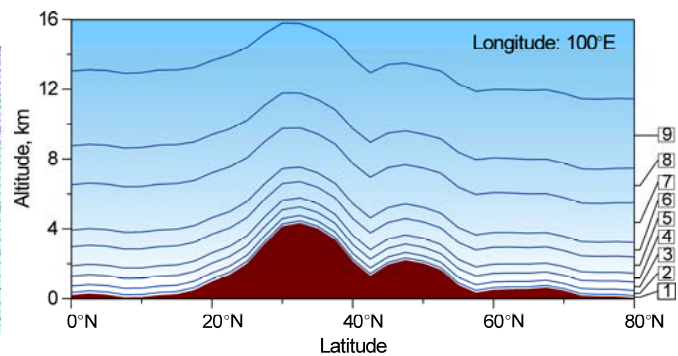


**Figure 2.2.** Vertical grid structure of the model domain. Nine terrain-following  $\sigma$ -levels: (1) –  $\sigma = 0.99$ ; (2) – 0.96; (3) – 0.91; (4) – 0.85; (5) – 0.77; (6) – 0.68; (7) – 0.55; (8) – 0.4; (9) – 0.26

In order to take into account the influence of the relief on the pollutant airborne transport the terrain-following  $\sigma$ -coordinate is employed in the vertical direction. The  $\sigma$ -coordinate is defined as a ratio of local atmospheric pressure  $p$  to the surface pressure  $p_s$ :

$$\sigma = \frac{p}{p_s}, \quad (2.1)$$

The vertical grid structure of the model domain is shown in Figure 2.2. It consists of nine  $\sigma$ -levels of variable thickness up to approximately 12-km altitude and has an open upper boundary.

## 2.1. Basic equations

The model is based on the three-dimensional advection-diffusion equation adapted to the  $\sigma$ -coordinate

$$\frac{\partial}{\partial t}(qp_s) = -\nabla_H \cdot (qp_s \mathbf{V}_H) - \frac{\partial}{\partial \sigma}(qp_s \sigma) + \frac{\partial}{\partial \sigma} \left[ K_\sigma \frac{\partial}{\partial \sigma}(qp_s) \right] + S - R. \quad (2.2)$$

Here  $q=c/\rho$  is a pollutant mixing ratio;  $c$  and  $\rho$  are the pollutant volume concentration and the local air density;  $\sigma=d\sigma/dt$  is the analog of vertical velocity for  $\sigma$ -coordinate;  $\nabla_H$  and  $\mathbf{V}_H$  denote horizontal divergence operator and horizontal wind velocity respectively. The effective diffusion coefficient  $K_\sigma$  is expressed through the vertical eddy diffusion coefficient  $K_z$  as follows

$$K_\sigma = \frac{g^2 \rho^2}{p_s^2} K_z, \quad (2.3)$$

where  $g$  is the gravitational acceleration. The local air density  $\rho$  can be derived from the equation of state:

$$\rho = \frac{p}{R_a T_a} = \frac{\sigma p_s}{R_a T_a}. \quad (2.4)$$

Here  $T_a$  and  $R_a$  are air temperature and the gas constant for humid air respectively.

Introducing a new variable  $\psi = qp_s$  we can abstract from the features of the  $\sigma$ -coordinate and operate with ordinary divergent form of the advection-diffusion equation:

$$\frac{\partial \psi}{\partial t} = -\nabla_H \cdot (\psi \mathbf{V}_H) - \frac{\partial}{\partial \sigma}(\psi \sigma) + \frac{\partial}{\partial \sigma} \left[ K_\sigma \frac{\partial \psi}{\partial \sigma} \right] + S - R. \quad (2.5)$$

However, restoring  $q$  from  $\psi$  one has to keep in mind that the surface pressure is changeable due to the air mass transfer and should satisfy the continuity equation:

$$\frac{\partial p_s}{\partial t} + \nabla_H \cdot (p_s \mathbf{V}_H) + \frac{\partial}{\partial \sigma}(p_s \sigma) = 0. \quad (2.6)$$

The first two terms on the right hand side of Equation (2.5) describe horizontal and vertical advection of a pollutant in the atmosphere. The third term represents vertical eddy diffusion, and the last two terms describe bulk pollutant sources (as emissions, physical and chemical transformations etc.) and removal processes. Because of the low grid resolution in horizontal direction ( $2.5^\circ \times 2.5^\circ$ ) horizontal eddy diffusion can be neglected in comparison with the artificial diffusion of the numerical scheme. Utilizing the time-splitting procedure [e.g. Yanenko, 1971; Marchuk, 1974; McRae et. al., 1982] all terms on the right hand side of the Eq. (2.5) can be considered separately and time integration of the appropriate processes are

performed successively. At the current stage of the model development only particulate form of the pollutant transport and deposition is considered. Chemical transformations of any specific pollutant lie beyond the scope of this stage and appropriate chemical modules are to be elaborated and included in further stages.

### 2.3. Horizontal advection

In spherical coordinate system the horizontal advective part of the Eq. (2.5) has the following form:

$$\frac{\partial \psi}{\partial t} = -\frac{1}{R_E \cos \varphi} \left[ \frac{\partial(\psi V_\lambda)}{\partial \lambda} + \frac{\partial}{\partial \varphi}(\psi V_\varphi \cos \varphi) \right], \quad (2.7)$$

where  $\lambda$  and  $\varphi$  are the geographical longitude and latitude;  $R_E$  is the Earth radius;  $V_\lambda$  and  $V_\varphi$  are zonal and meridional components of the wind speed respectively. Moreover, the former term in the square brackets describes the zonal advective transport, while the latter term presents the meridional one.

Equation (2.7) is solved by means of the flux-form advection Bott scheme [Bott, 1989a; 1989b]. It has been proved that this scheme is mass conservative, positive-definite, and is characterized by comparatively low artificial diffusion [see e.g. Dabdub and Seinfeld, 1994]. Further improvements of the original scheme version provide the scheme monotonicity and reduce the time-splitting error [Bott, 1992; 1993]. Besides, comparing to more precise but more computationally expansive advection algorithms as Accurate Space Derivative method and Galerkin method [Dabdub and Seinfeld, 1994], the Bott scheme does not require large computational capacities.

In order to apply the original Bott scheme [Bott, 1989a; 1989b] to the advection transport in the hemispheric model it has been adapted to the spherical coordinates. Detailed description of the Bott advection scheme in the spherical coordinates is presented in Annex A. The subgrid distribution of the variable  $\psi$  within the grid cells is approximated by polynomials of the second order. The distribution within the polar cell is approximated by a piecewise continuous surface consisting of a number of polynomial-shaped sectors divided by meridians and converging to the pole point.

To examine the performance of the constructed advection scheme the classical Smolarkiewicz numerical experiments [Smolarkiewicz, 1982] have been performed. In the first experiment initial distribution of  $\psi$  is transported in the uniform rotational flow. In the second one transformation of the initial distribution in the strong deformational flow is considered. In both numerical experiments cone-shaped initial distribution has been determined with  $\psi=110$  at the top and  $\psi=10$  at the bottom of the cone (arbitrary units).

### *Rotational flow*

The objective of the rotational flow experiment is to examine the model ability to simulate a pollutant horizontal advective transport and to evaluate artificial diffusion of the numerical scheme. The wind field of the rotational flow is shown in Figure 2.3 as well as the initial cone shaped distribution. The axis of the rotational flow is sloped down from the Earth axis with the angle  $30^\circ$  and the center of the initial distribution is located at the latitude  $20^\circ\text{N}$ . Since the flow is non-divergent the uniform distribution should remain uniform, while the cone-shaped one theoretically should be transported as a solid body. However, in reality the cone is smoothed down due to the artificial diffusion.

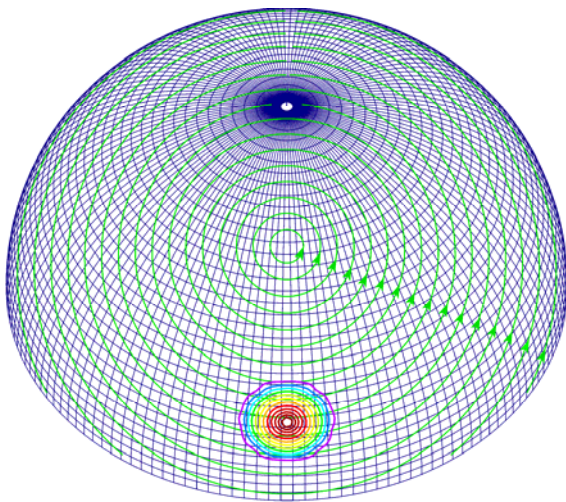


**Figure 2.3.** Conditions of the rotational flow numerical experiment: Wind streamlines and the initial cone-shaped distribution. Concentric circles denote isolines of  $\psi$  value with step  $\Delta\psi = 8$  (arbitrary units)

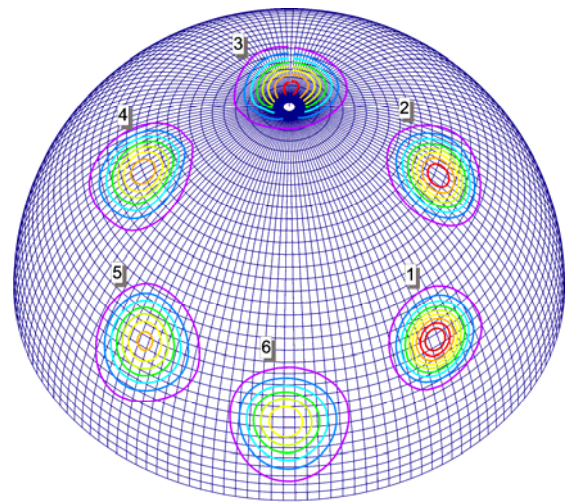


**Figure 2.4.** Results of the rotational flow numerical experiment. Concentric circles denote isolines of  $\psi$  value with step  $\Delta\psi = 8$  (arbitrary units): 1 – after  $1/6$  of the full revolution; 2 –  $1/3$ ; 3 –  $1/2$ ; 4 –  $2/3$ ; 5 –  $5/6$ ; 6 – after the full revolution

Results of the test are presented in Figure 2.4. The numbered sets of concentric circles show the cone location and shape at different moments of the revolution with time step  $\Delta t = 1/6$  of the whole revolution period. As seen from the figure the cone only slightly changes its shape due to numerical dispersion and artificial diffusion after the whole revolution. It has become lower (about 60% of the original height) and its circular shape has been somewhat disturbed. Thus, the advection scheme does not produce considerable distortions and has comparatively low artificial diffusion.

### *Deformational flow*

The objective of the deformational flow experiment is to examine the model stability in strong deformational flows and evaluate possible time-splitting error [Bott, 1993; Easter, 1993; Clappier, 1998]. The velocity field and the initial cone-shaped distribution for the

deformational flow experiment are presented in Figure 2.5 in spherical coordinates. Zonal and meridional components of the wind are determined by the following formulas:

$$V_{\lambda} = 4 \sin(4\lambda) \sin(4\varphi - \pi/2),$$

$$V_{\varphi} \cos \varphi = 4 \cos(4\lambda) \cos(4\varphi - \pi/2).$$

As it is seen from the figure the wind field is built up from sets of symmetrical vortices. Since the flow is non-divergent again a uniform distribution should remain uniform except zones where mass from the initial cone incoming. But anyway values of  $\psi$  should remain limited at any point of the domain.

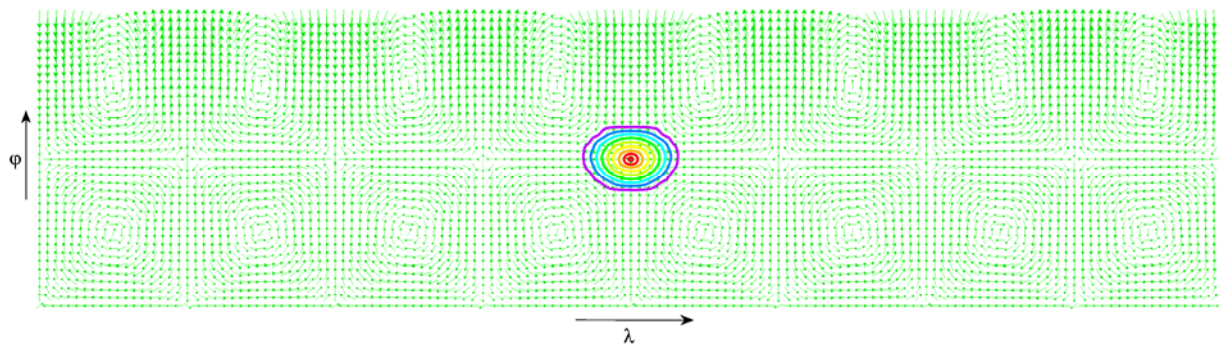


**Figure 2.5.** Conditions of the deformational flow numerical experiment: Wind velocity vectors and the initial cone-shaped distribution. Concentric circles denote isolines of  $\psi$  value with step  $\Delta\psi = 10$  (arbitrary units)

Results of the experiment are presented in Figure 2.6. Figure 2.6.a shows the initial cone-shaped distribution in the spherical coordinates. Figures 2.6.b–e illustrate transformation of the distribution in the deformation flow and correspond to different time moments (or different numbers of iterations). As one can see the mass is coming along the boundaries of the vortices and is penetrating to the neighboring ones. The main difference from the original deformational flow experiment [Smolarkiewicz, 1982] is sharing of the mass between the remote vortices through the pole (see Fig. 2.6.d). This is peculiar feature of the spherical geometry. The maximum value of  $\psi$  distribution decreases in time, that is the model is stable to the deformational flow. Besides, there is no observable time-splitting error.

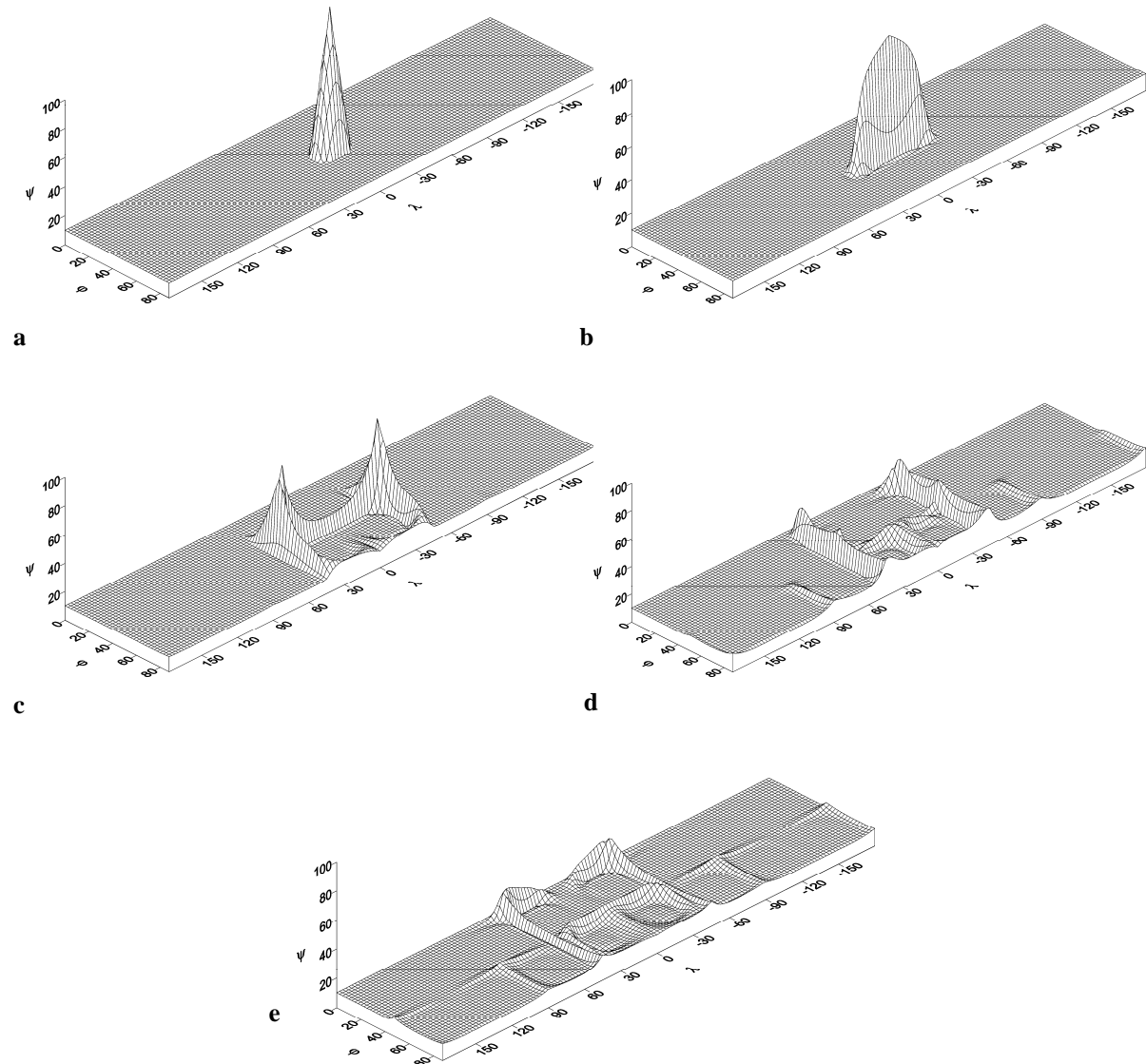


**Figure 2.6:** Results of the deformational flow numerical experiment  $\psi$  distribution: (a) – initial; (b) – after 130 iterations; (c) – 390 iterations; (d) – 650 iterations; (e) – 810 iterations

## 2.4. Vertical advection

The vertical advection part of Equation (2.5) has the following form:

$$\frac{\partial \psi}{\partial t} = -\frac{\partial}{\partial \sigma}(\psi \sigma). \quad (2.8)$$

This one-dimensional advection equation is solved by means of the ordinary second-order Bott scheme generalized for a grid with variable step  $\Delta\sigma$ . The analog of vertical velocity  $\sigma$  is calculated from Equation (2.6). For this purpose one should integrate the equation over a closed three-dimensional cell from the ground to the upper boundary and use the boundary condition at the surface  $\sigma_s = 0$ . Moreover, to calculate fluxes through the lateral faces one

should apply the standard procedure of the Bott scheme (see expressions (A.5) and further discussion in Annex A) applied to the surface pressure.

To examine the vertical advective transport in combination with the horizontal one a number of numerical experiments have been performed. One of them is presented below. Two-dimensional advective transport is considered. Conditions and results of the experiment are shown in Figure 2.7. The real orography corresponding to 100°E longitude is utilized as a underlying surface. To simulate straight-line transport of the initial distribution in the terrain-following coordinates the uniform wind field has been determined along the horizon (see Fig. 2.7.a). For this purpose we had to apply unrealistic “transparent” boundary conditions at the surface: The wind can freely flow in and out through the surface. The main objective of the experiment is to examine the model ability to adequately simulate the advective transport in the atmosphere without influence of the curvilinear sigma coordinate. The cone-shaped initial distribution is determined in the left side of the domain (see Fig. 2.7.b) and moves to the right. As one can see from the figure the cone is transported along straight line, and somewhat smoothing of the initial shape is observed due to the artificial diffusion. The originally circular shape is slightly disturbed because of the non-uniform grid.

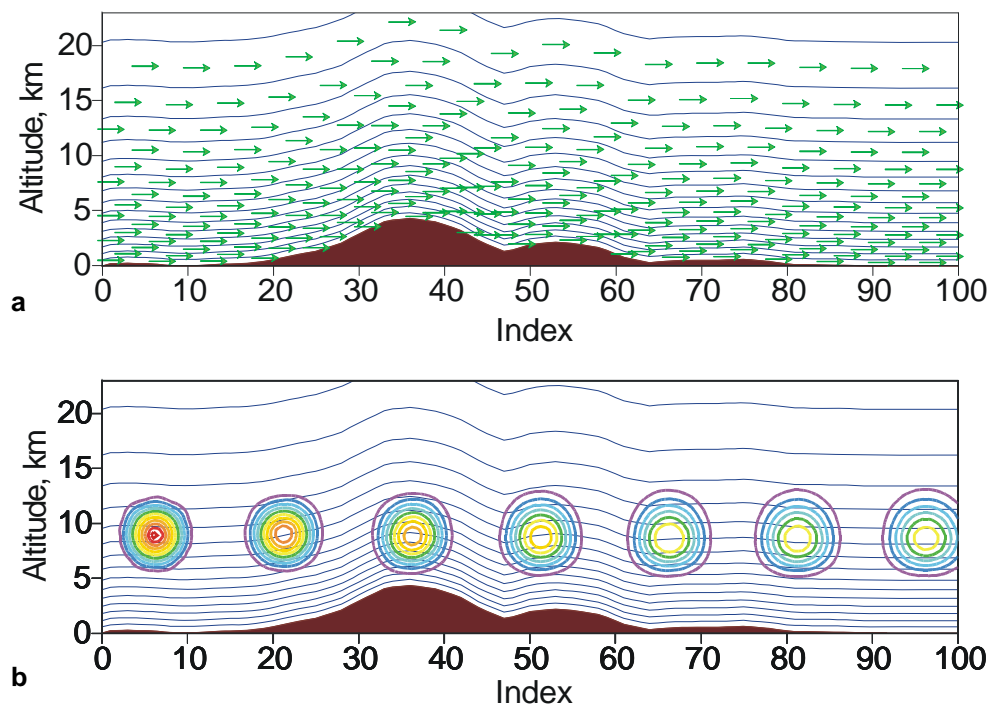


**Figure 2.7.** Wind field (a) and results (b) of the numerical experiment for the vertical advection

## 2.5. Vertical diffusion

Vertical diffusion is described by the following equation (see Equation 2.5):

$$\frac{\partial \psi}{\partial t} = \frac{\partial}{\partial \sigma} \left[ K_{\sigma} \frac{\partial \psi}{\partial \sigma} \right]. \quad (2.9)$$

The diffusion equation (2.9) has been approximated by the second-order implicit numerical scheme in order to avoid restrictions of the time step caused by possible sharp gradients of  $\psi$ . To take into account the dry deposition flux the following boundary condition was applied at the surface:

$$-K_{\sigma} \frac{\partial \psi}{\partial \sigma} \Big|_{\sigma=1} = V_d \psi, \quad (2.10)$$

where  $V_d$  is the dry deposition velocity. The obtained system of linear algebraic equations is solved by means of the sweep method.

## 2.6. Removal processes

Removal processes have been parameterized on the base of semi-empirical approach utilized in the operational MSCE-HM model [Ryaboshapko *et al.*, 1999]. As it was mentioned above only particulate form of the pollutant is considered at the current stage of the model development.

Dry uptake of the pollutant by the underlying surface is taking into account by introduction of the appropriate boundary conditions (2.10) for the diffusion equation (2.9). The dry deposition velocity is determined for monodisperse aerosol particles with characteristic mass median diameter (0.55 for lead) and depends on the friction velocity ( $u_*$ , [m/sec]) of the atmospheric boundary layer and roughness of the underlying surface ( $z_0$ , [m]) according the following expressions (for lead):

$$V_d^{land} = (0.02u_*^2 + 0.01)(z_0 \cdot 10^3)^{0.33}, \text{ [cm/sec]} \quad (2.11)$$

$$V_d^{sea} = 0.15u_*^2 + 0.013, \text{ [cm/sec]}$$

Wet removal is parameterized by means of the washout ratio approach. Washout of aerosol particles is described by the following first-order equation:

**Table 2.1.** Temporal variation of the washout ratio for lead

Month	$W$
January	$3.1 \cdot 10^5$
February	$3.1 \cdot 10^5$
March	$3.8 \cdot 10^5$
April	$3.9 \cdot 10^5$
May	$5.0 \cdot 10^5$
June	$5.0 \cdot 10^5$
July	$3.8 \cdot 10^5$
August	$3.0 \cdot 10^5$
September	$3.1 \cdot 10^5$
October	$1.9 \cdot 10^5$
November	$1.7 \cdot 10^5$
December	$2.7 \cdot 10^5$

$$\frac{\partial q}{\partial t} = -\frac{WI_p g \sigma}{R_a T_a \Delta \sigma} q, \quad (2.12)$$

where  $q$  is the pollutant mixing ratio;  $W$  is the washout ratio;  $I_p$  is the precipitation intensity. Temporal variation of the washout ratio was derived on the base of the available monitoring data [Ryaboshapko *et al.*, 1999] and is presented in Table 2.1.

### 3. Meteorological and emission data

To supply the model with meteorological data the System of Diagnostics of the low Atmosphere (SDA) has been elaborated in co-operation with Hygrometeorological Centre of Russia. The system provides a complete set of meteorological data with 6-hour temporal resolution and parametrization of the atmospheric boundary layer. The list of meteorological parameters delivered by SDA is presented in Table 3.1 along with their characteristics.

As it was mentioned in above the hemispheric model is mostly developed to evaluate the atmospheric dispersion of such volatile pollutants as mercury and some POPs. However, their airborne transport is accompanied by involved physical and chemical transformations. Therefore, it is reasonable to perform verification of the model transport and deposition characteristics on the base of a pollutant simpler for interpretation like lead. Lead is emitted and transported through the atmosphere mainly in the particle-bounded form and practically does not undergo any aggregate state transformation.

In our calculations we utilized anthropogenic emission data based on the GEIA Global Lead Emission Inventory for 1989 [Pacyna et al., 1995]. The original global data with spatial resolution  $1^\circ \times 1^\circ$  have been redistributed to the intrinsic model grid. The resulting anthropogenic emission density of lead in the Northern Hemisphere is presented in Figure 3.1. As it is seen from the figure the most significant emission

**Table 3.1.** Meteorological parameters supplying by the System of Diagnostics of the low Atmosphere (SDA)

Parameter	Notation	Type
Wind velocity	$V_\lambda, V_\varphi$	bulk
Air temperature	$T_a$	bulk
Vapour mixing ratio	$Q_v$	bulk
Precipitation intensity	$I_p$	bulk
Surface pressure	$p_s$	surface
Large-scale cloudiness	$C_L$	bulk
Convective cloudiness	$C_C$	bulk
Surface temperature	$T_s$	surface
Vertical eddy diffusion coefficient	$K_z$	bulk
Roughness of the underlying surface	$z_0$	surface
Soil moisture	$M_s$	surface
Snow cover height	$h_s$	surface

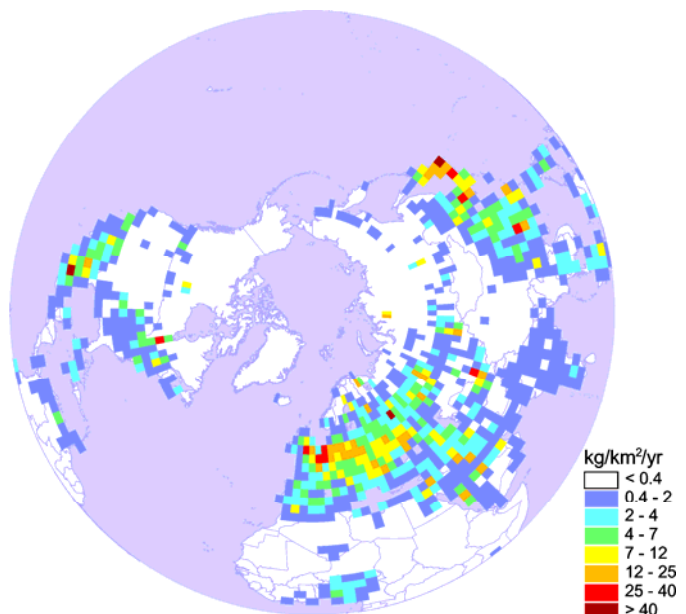


**Figure 3.1.** Anthropogenic emission density of lead in 1989 based on GEIA inventory (spatial resolution  $2.5^\circ \times 2.5^\circ$ )

sources are in Europe, Eastern Asia, and North America. The total emissions of lead from the Northern Hemisphere are as much as  $1.8 \times 10^5$  tonnes per year.

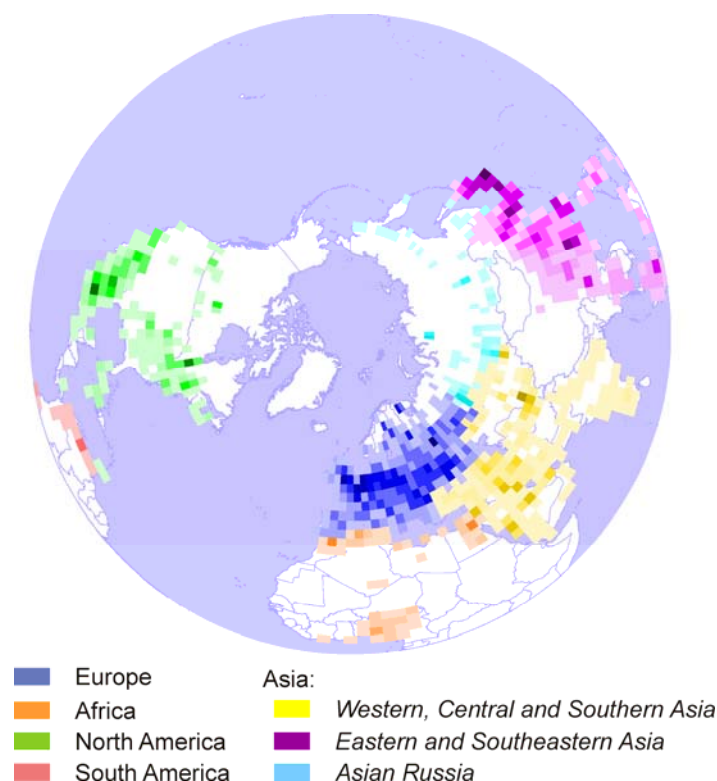


**Figure 3.2.** Division of the lead emission field into the continents (intensity scales the same as in Fig. 3.1)

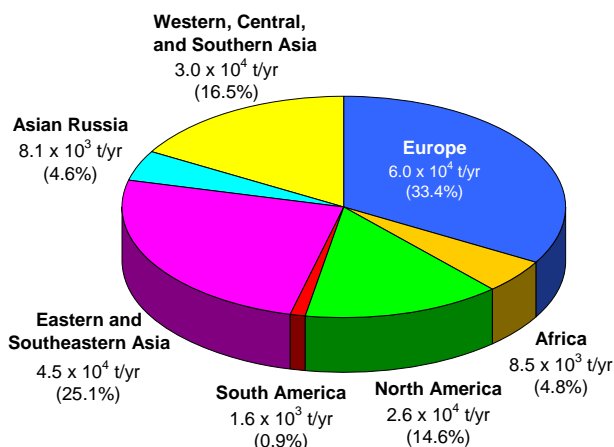


**Figure 3.3.** Relative contributions of different continents and regions to the total emissions of lead

In order to calculate the deposition from different continents and regions the whole hemispheric emission field has been divided into several areas including emission sources related to the continents (see Fig. 3.2): Europe, Africa, North America, South America, and Asia. Moreover, the last one has been subdivided into three regions: Western, Central, and Southern Asia; Eastern and South-eastern Asia; and Asian Russia. Relative contributions of each continent or region to the total emissions of lead are presented in Figure 3.3. According to the pie chart the main emitters of anthropogenic lead in the Northern Hemisphere are Asia ( $8.2 \times 10^4$  t/yr) and Europe ( $6 \times 10^4$  t/yr), which contribute almost 80% of the total lead emissions.

#### 4. Model verification

Complete hemispheric model requires to be verified against some reliable results of other models or measurements. First of all we compared modelling results obtained by the hemispheric model with those by regional MSCE-HM model of heavy metal atmospheric transport. The MSCE-HM model has been developed and employed in operational regime for

the last several years. It has been verified in a number of intercomparison campaigns with other regional models [Sofiev *et al.*, 1996; Gusev *et al.*, 2000; Ryaboshapko *et al.*, 2001] and has been qualified by means of sensitivity and uncertainty studies [Travnikov, 2000]. Thus its results can be considered as quite reliable within European region. In the other verification procedure the hemispheric model results were compared with measurement data available within the EMEP monitoring network. In both cases lead airborne transport was considered.

#### 4.1. Comparison with regional MSCE-HM model

The regional MSCE-HM model is a three-dimensional Eulerian-type model operating within the EMEP domain (see Fig. 4.1). The model grid covers whole Europe, the Mediterranean Sea, and part of the Atlantic Ocean with spatial resolution 50 km × 50 km. In the vertical it consists of 5 atmospheric layers up to approximately 4 km. Detailed description of the model can be found in [Ryaboshapko *et al.*, 1999].

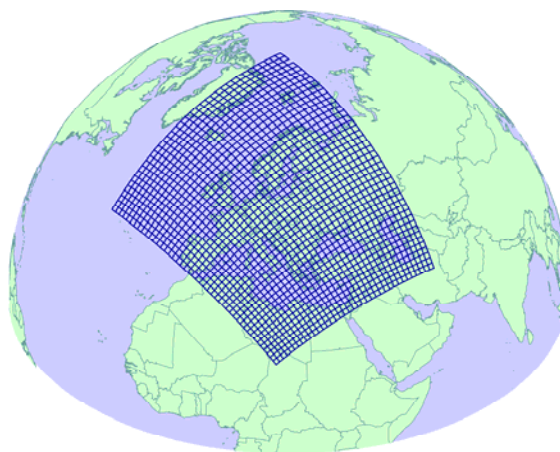


**Figure 4.1.** Computation domain of the regional MSCE-HM model (EMEP domain)

Conditions of the comparison are summarized in Table 4.1. Both models were employed to calculate the long-range transport and deposition of anthropogenic lead in 1990. Each model used its own computation domain and spatial resolution. In both cases we used meteorological data for 1990. The MSCE-HM model utilized

official anthropogenic emission data from the EMEP inventory while the hemispheric model operated with the GEIA Global Lead Emission Inventory for 1989 [Pacyna *et al.*, 1995]. Only European emission sources were considered from the whole hemispheric field. Since the official EMEP data considerably differ from the GEIA inventory, we had to reduce the latter by multiplying the emission field by a correction factor ( $\sim 0.6$ ) to equalize the total emissions from Europe in both cases. The spatial fields of lead anthropogenic emission density for regional MSCE-HM and hemispheric models are presented in Figures 4.2 and 4.3 respectively.

**Table 4.1.** Conditions of the hemispheric and regional MSCE-HM models comparison study

Characteristics	Hemispheric model	MSCE-HM model
Objective	Lead long-range transport and deposition in 1990	
Computation domain	Northern Hemisphere	EMEP domain
Spatial resolution	2.5° × 2.5°	50 km × 50 km
Meteorological data	for 1990	for 1990
Emission data	Reduced GEIA inventory for 1989	Official data from the EMEP inventory for 1990

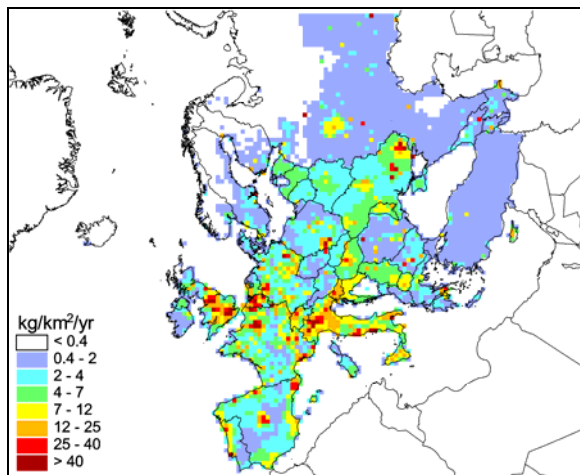


**Figure 4.2.** Lead anthropogenic emission density in 1990 (official data from the EMEP inventory)

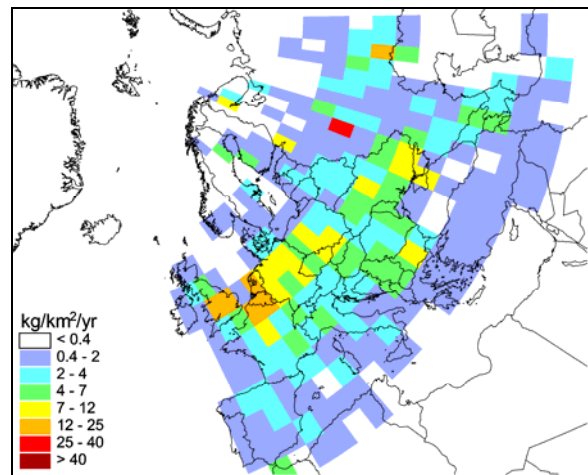


**Figure 4.3.** Lead anthropogenic emission density in 1989 (reduced GEIA Inventory)

As seen from the figures, considerably lower resolution of the hemispheric model leads to rougher distribution of the anthropogenic emissions smoothing all emission peaks (Fig. 4.3). Besides, the emission fields have some spatial distinctions. First of all one has to mention significantly higher emission levels for the regional model (Fig. 4.2) in Northern Italy and in Spain.

Results of the model comparison are presented in Figures 4.4 – 4.9. Figures 4.4 and 4.5 show spatial distributions of mean annual lead concentration in surface air obtained by the MSCE-HM and hemispheric models respectively.

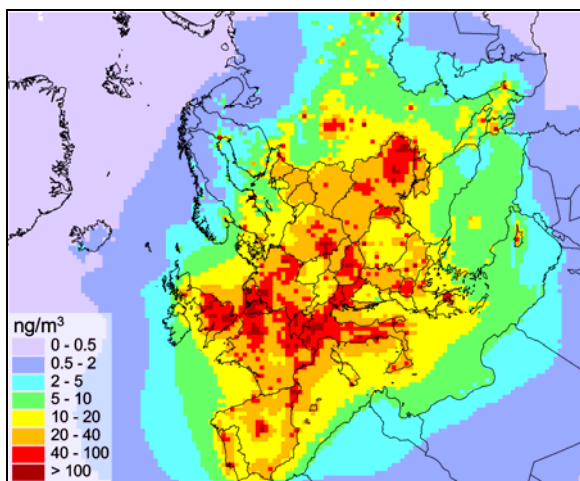


**Figure 4.4.** Spatial distribution of mean annual lead concentration in the surface air obtained by the regional MSCE-HM model

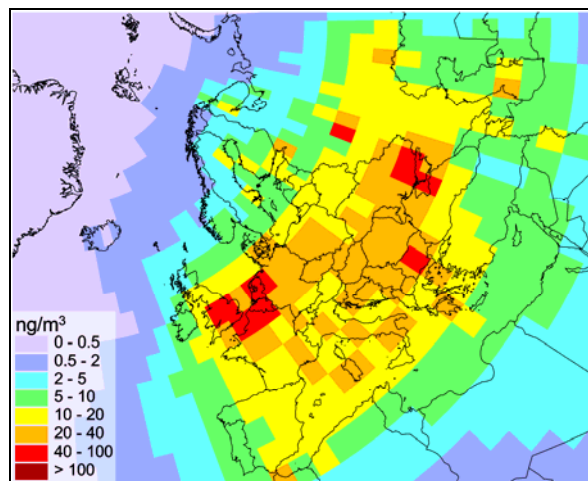


**Figure 4.5.** Spatial distribution of mean annual lead concentration in the surface air obtained by the hemispheric model

Here one should take into account that the models have quite different advection schemes, spatial resolutions, and utilize different emission data. Nevertheless, the spatial distribution

fields in both cases look quite similar. The regions with the highest lead concentrations coincide as a whole, except several regions (e.g. Northern Italy, Spain etc.), where the hemispheric model produce considerably lower values. The reason for the distinction is different emission fields for the regional and hemispheric models as it was mentioned above (compare Fig. 4.1 and 4.2). The models produce very close background lead concentrations in air far from industrial regions (e.g. the Atlantic Ocean and the Arctic) characterizing long-range lead transport. It is natural that the concentration field of the hemispheric model is smoother (without significant peaks) than that of the regional one due to lower spatial resolution. Besides, the hemispheric model predicts more considerable lead transport outside the domain eastward and south-eastward. A similar situation is for the spatial distributions of total annual lead deposition (compare Fig. 4.6 and 4.7).

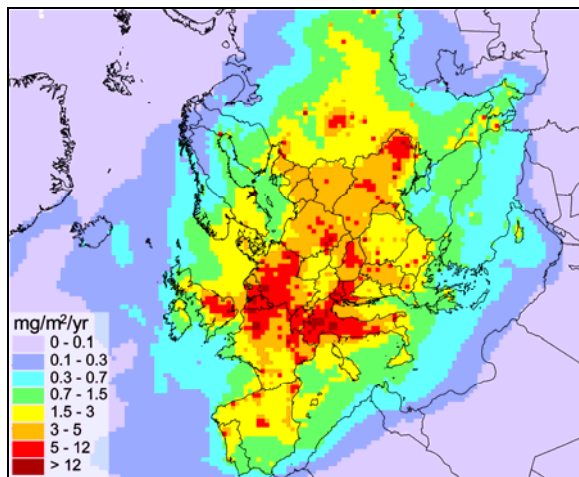


**Figure 4.6.** Spatial distribution of total annual lead deposition obtained by the **regional MSCE-HM model**

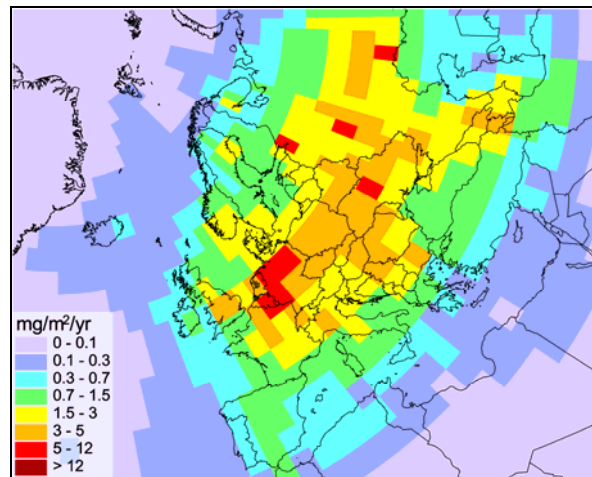


**Figure 4.7.** Spatial distribution of total annual lead deposition obtained by the **hemispheric model**

Quantitative comparison of the concentration and deposition fields obtained by the regional and hemispheric models has been performed by means of regression analysis and is presented in Figures 4.8 and 4.9. We compared values of mean annual lead concentration in air (Fig. 4.8) and total annual lead deposition (Fig. 4.9) obtained by both models at grid points of the EMEP domain. To avoid excessive overloading of the figures we present only one sixth of all the grid cells uniformly distributed over the domain. As seen from the figures the slopes of the regression line are quite close to unity (solid blue line) and correlation coefficients ( $R$ ) are higher than 0.7 in both cases. The significant overshoots of the regional model results can be explained by considerably higher resolution and correspond to points with the highest emission. As a whole the most points are within a “factor of two” limits (dashed blue lines).

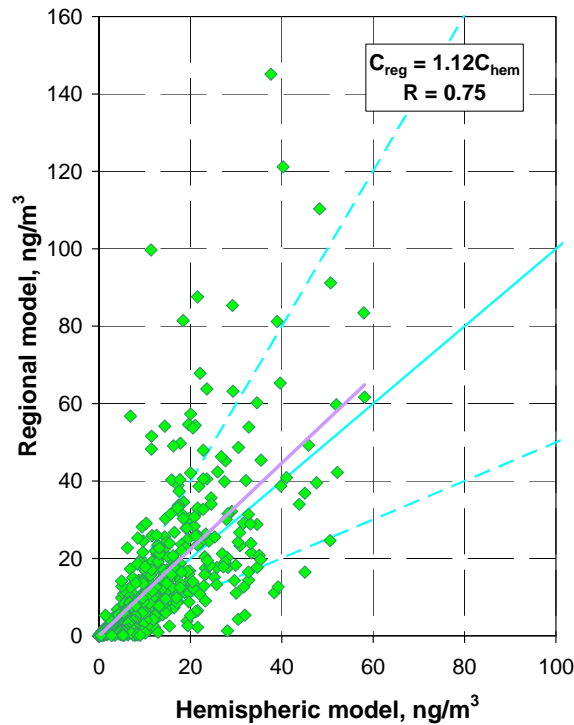


**Figure 4.8.** Comparison of the mean annual lead concentration fields obtained by the regional MSCE-HM and hemispheric models. Equation  $C_{reg} = AC_{hem}$  describes the regression line with the slope  $A$ ;  $R$  is the correlation coefficient

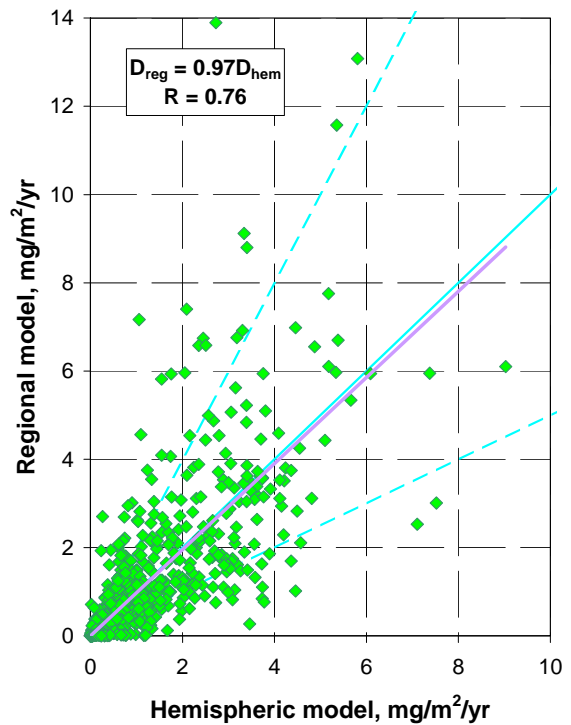


**Figure 4.9.** Comparison of the annual total lead deposition fields obtained by the regional MSCE-HM and hemispheric models. Equation  $D_{reg} = AD_{hem}$  describes the regression line with the slope  $A$ ;  $R$  is the correlation coefficient

#### 4.2. Comparison with measurements

In order to verify the hemispheric model consistency we also compared the modelling results with the available measurements. The original (not reduced) emission data for lead in 1989 from the GEIA Inventory [Pacyna *et al.*, 1995] were used for the modelling. The measurement data for lead in 1989 were taken from the EMEP monitoring network [Berg *et al.*, 1996]. The comparison of the observed and modelled mean annual lead concentrations in the surface air and annual wet deposition fluxes are presented in Figures 4.10 and 4.11 respectively. As seen from the figures the modelling results are in a satisfactory agreement with observations in both cases. The model overestimates the observed air concentrations at the most monitoring stations (see Fig. 4.10). As one can see from the regression analysis (Fig. 4.10.b and 4.11.b) the discrepancy of the modelling results and measurements mostly does not exceed a factor of two. However, it should be noticed that the comparison undertaken cannot adequately characterize the model consistency because the available monitoring data are presented only by European stations. For more comprehensive analysis additional measurements should be involved from other regions (North America, Asia, the Arctic etc.)

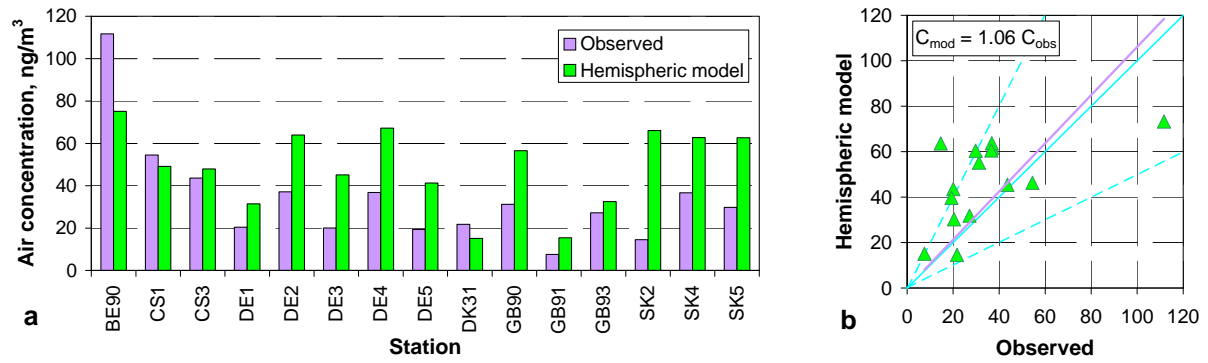


Figure 4.10. Observed and modelled mean annual lead concentrations in the surface air,  $\text{ng/m}^3$

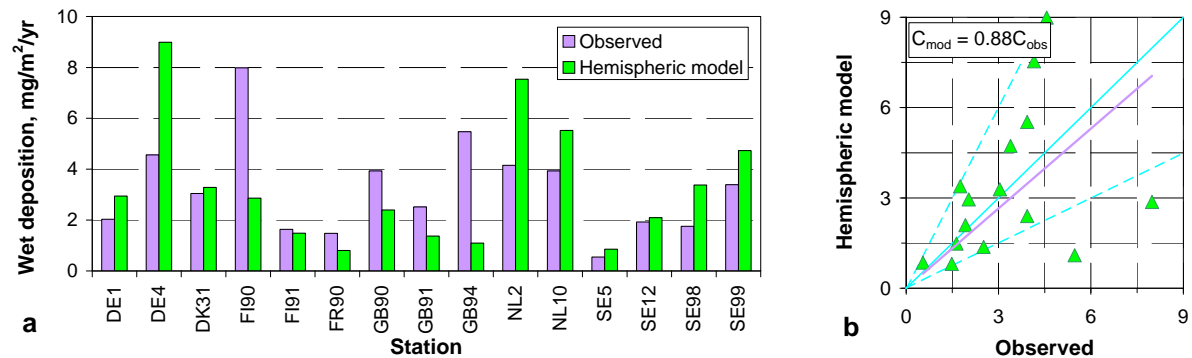


Figure 4.11. Observed and modelled annual wet deposition fluxes,  $\text{mg/m}^2/\text{yr}$

## 5. Preliminary results of lead airborne transport modelling

Here we present preliminary results of lead long-range transport in 1990 obtained by the hemispheric model elaborated. It should be reminded that we consider only *anthropogenic* lead emission neglecting natural sources such as wind erosion, volcanic activity, sea salt spray etc. [Nriagu, 1989]. The natural component of transported lead hardly plays a significant role in the contaminated environment of industrial regions. However, it can be significant in remote comparatively clean areas.

### 5.1. Air concentration and deposition fields

Figure 5.1 shows spatial distribution of mean annual lead concentration in the surface air over the Northern Hemisphere in 1990. It is not surprising that the most contaminated regions are those with the highest emission intensity (in Europe, Middle East, Eastern Asia, and in the south part of North America), where air concentration of lead exceeds  $40 \text{ ng/m}^3$  (one should realize that concentration and deposition values presented here are averaged over the cell  $2.5^\circ \times 2.5^\circ$ ). Besides, it is clearly seen that lead from anthropogenic sources

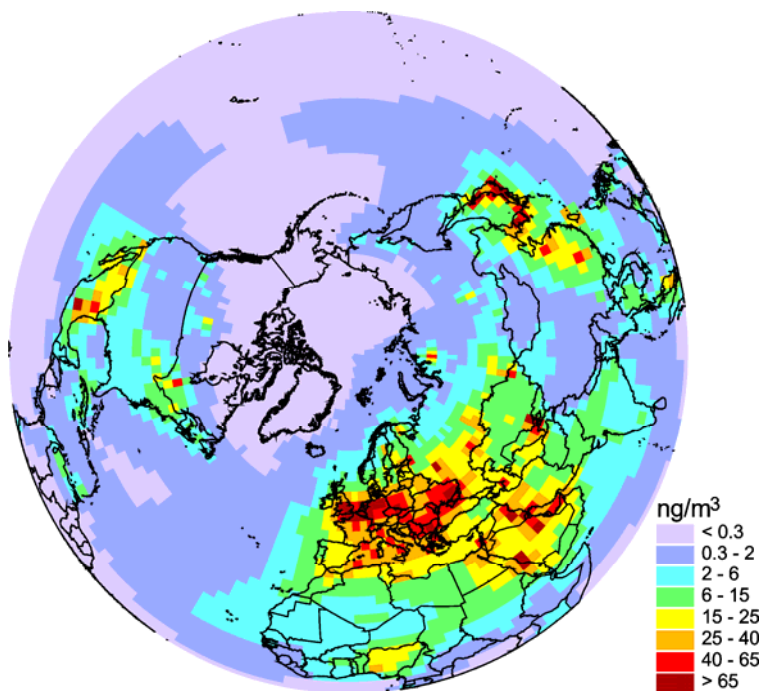


**Figure 5.1.** Spatial distribution of mean annual lead concentration in the surface air over the Northern Hemisphere in 1990

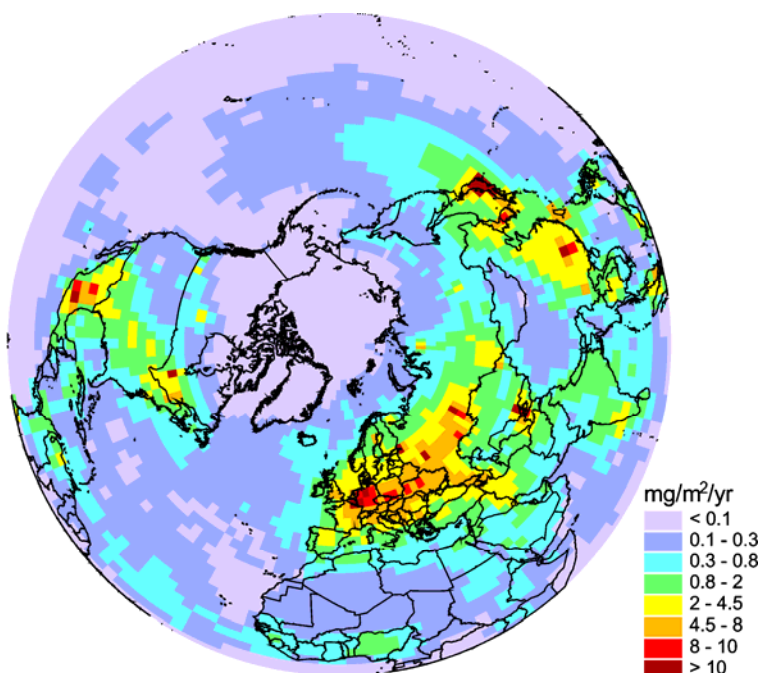


**Figure 5.2.** Spatial distribution of annual total lead deposition over the Northern Hemisphere in 1990

covers practically the whole Atlantic and partly the Western and Eastern Pacific. The lowest concentrations of anthropogenic lead are observed in the Arctic and Equatorial Pacific.

A similar situation is for lead deposition. Figure 5.2 presents spatial distribution of annual total lead deposition over the Northern Hemisphere in 1990. The deposition flux of anthropogenic lead varies from more than 10 mg/m<sup>2</sup>/yr in highly polluted regions to less than 0.05 mg/m<sup>2</sup>/yr in the Arctic. As a whole the deposition field looks more variegated due to significant influence of the annual precipitation amount on the pollutant deposition. There are well pronounced areas of higher deposition fluxes in South India and Equatorial Atlantic caused by big annual precipitation amount in these regions.

## 5.2. Deposition from the continents and regions

To understand the pathways of lead transport in the atmosphere we calculated deposition fields from different continents and regions. For this purpose we divided the whole hemispheric emission field into areas with sources related to different continents as it was described in Section 3. Total annual lead deposition from different continents and regions taken separately is presented in Figure 5.3. As seen from Figure 5.3.a the main pathways of anthropogenic lead transport from **Europe** are eastward, through all Eurasia to the Pacific

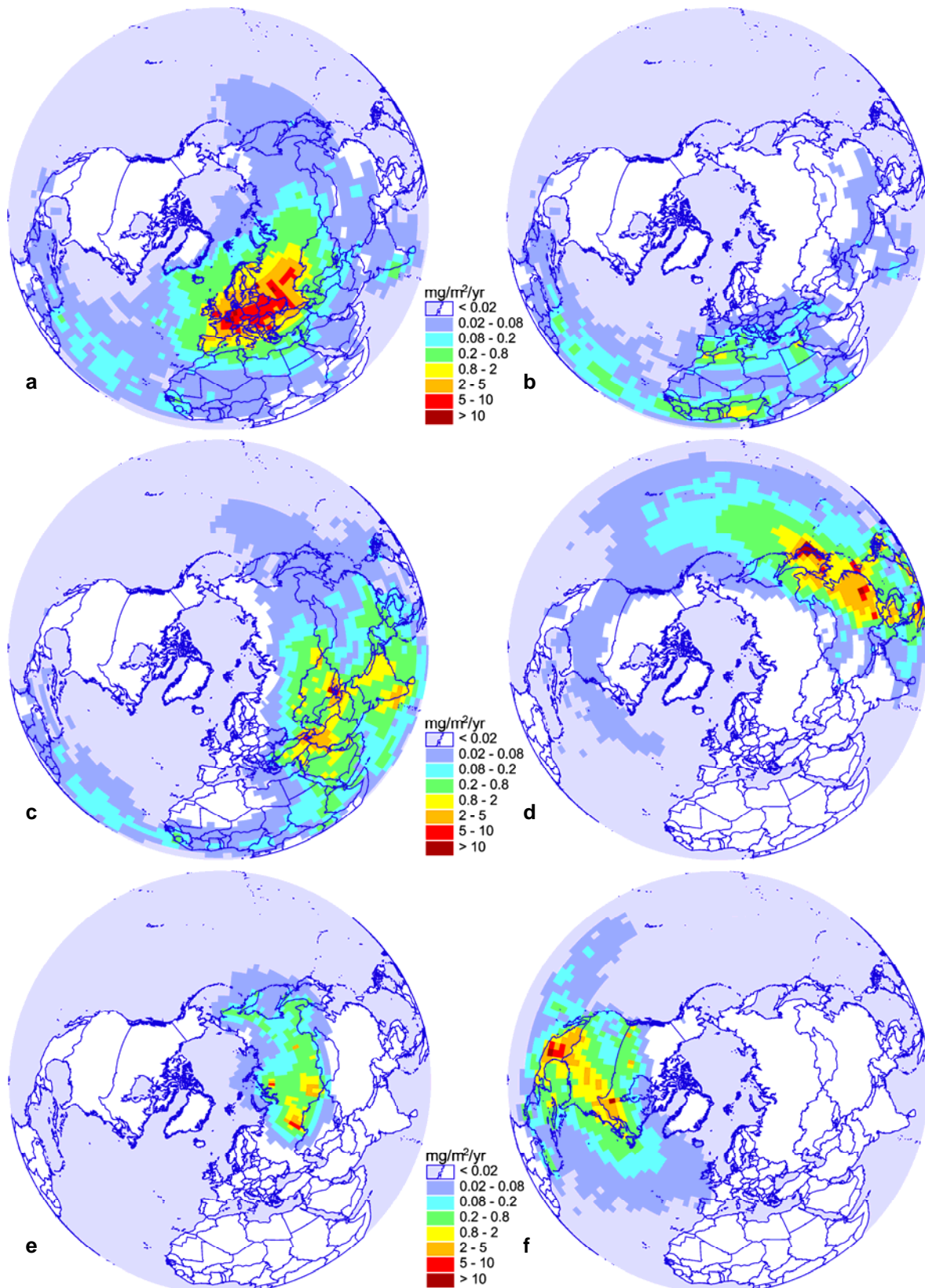


**Figure 5.3.** Total annual lead deposition from different continents and regions: (a) – from Europe; (b) – from Africa; (c) – from Western, Central, and Southern Asia; (d) – from Eastern and Southeastern Asia; (e) – from Asian Russia; (f) – from North America

Ocean, and south-westward to the Equatorial Atlantic. Considerable deposition from European sources is also to the Northern Atlantic. The main part of lead emitted from **Africa**

is transported westward along the Equator. As seen from Figure 5.3.b there is no significant flux of anthropogenic lead from Africa to Europe. **Western, Central and Southern Asia** region also produces zonal flux of lead through all Africa to the Equatorial Atlantic (Fig. 5.3.c). Besides it considerably contributes to lead deposition to the Indian Ocean. The main pathway of lead transport from **Eastern and Southeastern Asia** region is to the Pacific Ocean. Moreover, as one can see from Figure 5.3.d anthropogenic lead from Eastern Asia can come through all North America and reach the Atlantic Ocean. Due to peculiar properties of the atmosphere circulation over northern part of Asia there is no wide dispersion of lead from **Asian Russia** (see Fig. 5.3.e). The main pathways from this region are to the Arctic and the Northern Pacific. Figure 5.3.f shows that anthropogenic lead from **North America** is mostly transported to the Eastern Pacific and to the Atlantic Ocean. However, only a small amount of lead from North America can reach Europe.

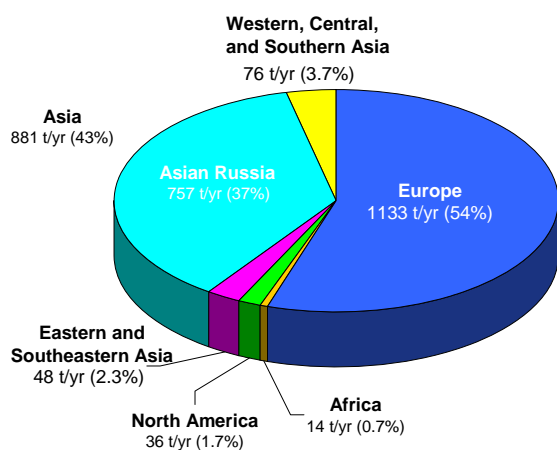


**Figure 5.4.** Total annual deposition to the Arctic from different continents

To illustrate the long-range pollution of remote regions by anthropogenic lead from different continents we have calculated relative contribution of the continents to the Arctic contamination. Figure 5.4 shows total annual deposition to the Arctic (within the Arctic Circle) from different continents. As it is seen from the figure the largest contribution is from European emission sources (54%). Although total emission from Asian Russia is comparatively small (see Fig. 5.4), its geographical location results in significant

contribution to the Arctic pollution (37%). Contribution of other continents does not exceed several per cent.

### 5.3. Vertical distribution of lead concentration in air

To illustrate the model ability to simulate processes of the pollutant lifting up, mixing, transport in the atmosphere and deposition to the surface we also calculated vertical distribution of lead concentration in the troposphere. Directions of the calculated vertical concentration profiles are shown in Figure 5.5. All profiles are going along meridians from the Pole to the Equator. The first one is coming through Europe and Africa (7.5°E), the second – through Eastern Asia (140°E), and the third – through North America (100°W). These vertical atmospheric profiles are presented in Figure 5.6.

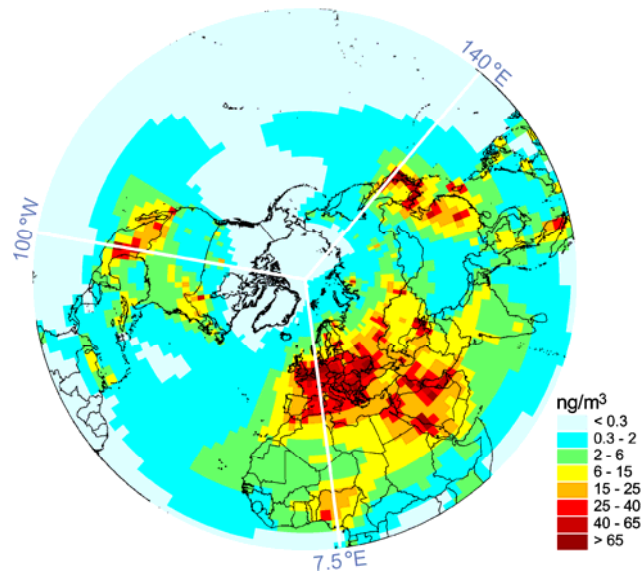


**Figure 5.5.** Mean annual lead concentration in the surface air. Lines show directions of the vertical atmospheric cross sections along the meridians: 7.5°E, 140°E, and 100°W

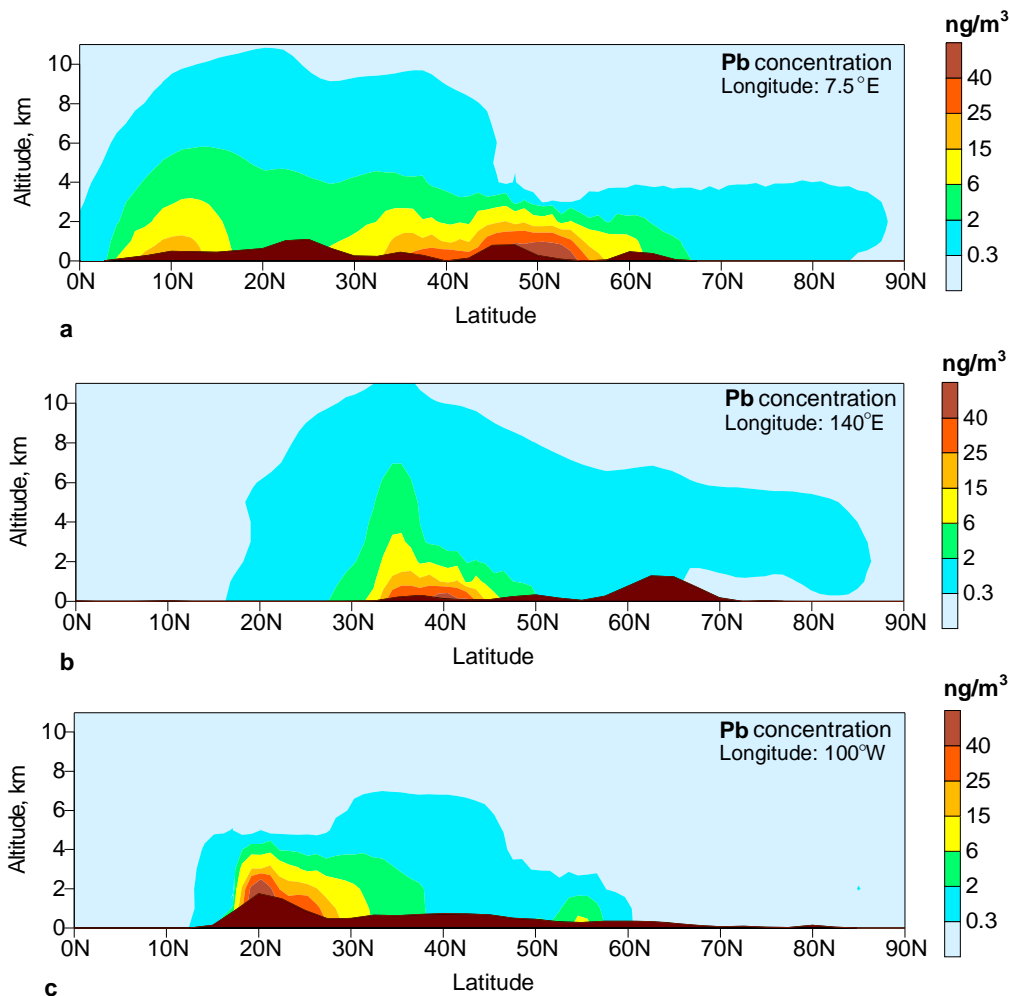


**Figure 5.6.** Vertical profiles of mean annual lead concentration in the atmosphere going along the meridians: (a) – 7.5°E; (b) - 140°E; (c) - 100°W.

Figure 5.6.a shows vertical concentration profile coming through Europe and Africa. As it is seen from the figure the highest concentrations correspond to emission sources located in Europe (42°N - 55°N) and Western Africa (around 10°N). More significant mixing of the tropospheric air in the lower latitudes leads to higher lifting of the pollutant in the atmosphere. On the other hand, comparatively small precipitation amount in the higher latitudes hinders the pollutant from significant wet removal and results in faraway transport northward. Figure 5.6.b presents vertical profile coming through Eastern Asia. The most significant sources in this direction are located in Japan (35°N - 42°N). There is also high lifting of the pollutant due to significant mixing in the low latitudes over the polluted regions. Stable atmosphere of the high latitudes prevents airborne transported lead from coming down and causes decrease of lead concentration near the surface due to dry uptake. The profile coming through North America is shown in Figure 5.6.c. The most significant emissions here relate to Mexican sources (18°N - 25°N). As one can see from the figure there is no observable flux of lead northward.

## 6. Conclusions

The hemispheric model of the airborne pollutant transport is currently under development in EMEP/MSCE. The model is related to the family of three-dimensional Eulerian-type models and operates in the spherical (geographical) coordinates. At the first stage of the model development the atmospheric transport module has been elaborated. It is based on the flux-form Bott advection scheme adapted to the spherical coordinates. The main removal processes have been parameterized in accordance with the semi-empirical approach used in the operational MSCE-HM model.

The elaborated model has been thoughtfully tested and verified. Testing of the advection scheme has shown that the model can adequately simulate pollutant transport in the atmosphere and does not produce significant numerical errors and distortions. The complete hemispheric model has been compared with the regional MSCE-HM model. The comparison has demonstrated that modelling results obtained by the hemispheric model are in satisfactory agreement with those of the regional one within European region. The hemispheric modelling results have also been compared with the available measurements. It has been shown that the observed and modelled values agree within a factor of two.

Preliminary results of lead airborne transport over the Northern Hemisphere have been obtained and discussed. Spatial distribution fields of mean annual lead concentration and total annual deposition have been calculated. Deposition fields from different continents and regions have been also evaluated in order to assess the main pathways of lead transport in the atmosphere. Vertical profiles of lead concentration in the atmosphere have been computed as well.

Further stages of the model development are to include adaptation of the model to the airborne transport of mercury and selected POPs (lindane, PCB etc.) as well as elaboration of the chemical and deposition modules for these pollutants on the base of the multi-compartment approach to the environmental pollution assessment. It is also planned to extend the model to the global level with the finer resolution ( $1^{\circ}\times 1^{\circ}$ ).

### ***Acknowledgements***

The author is very thankful to Dr. Alexey Ryaboshpko, Mr. Ilya Ilyin, Dr. Alexander Malanichev, and Mr. Michael Fedyunin for the valuable criticism of the manuscript and numerous advises. He is grateful to Prof. Victor Shatalov for the close attention to the work and fruitful discussions. And special thanks to Mrs. Larissa Zayavlina for thorough editing the text as well as to Ms. Irina Strizhkina and Mrs. Svetlana Yevdokimova for its preparing and publishing.

## References

- Berg T., Hjellbrekke A.-G., and Skjelmoen J. E. [1996] Heavy metals and POPs within the ECE region. EMEP/CCC Report 8/96, Norwegian Institute for Air Research, Kjeller, Norway.
- Bott A. [1989a] A positive definite advection scheme obtained by nonlinear renormalization of the advective fluxes. *Monthly Weather Review* **117**, 1006-1015.
- Bott A. [1989b] Reply to comment on "A positive definite advection scheme obtained by nonlinear renormalization of the advective fluxes." *Monthly Weather Review* **117**, 2633-2636.
- Bott A. [1992] Monotone flux limitation in the area-preserving flux-form advection algorithm. *Monthly Weather Review* **120**, 2592-2602.
- Bott A. [1993] The monotone area-preserving flux-form advection algorithm: Reducing the time-splitting error in two-dimensional flow fields. *Monthly Weather Review* **121**, 2637-2641.
- Clappier A. [1998] A correction method for use in multidimensional time-splitting advection algorithms: Application to two- and three-dimensional transport. *Monthly Weather Review* **126**, 232-242.
- Dabdub D., Seinfeld J. H. [1994] Numerical advective schemes used in air quality models – sequential and parallel implementation. *Atmospheric Environment* **28**, 3369-3385
- Easter R. C. [1993] Two modified versions of Bott's positive-definite numerical advection scheme. *Monthly Weather Review* **121**, 297-304.
- Gusev A., Ilyin I., Petersen G., van Pul A., Syrakov D., and Pekar M. [2000] Long-range transport model intercomparison studies. EMEP/MSC-E Technical note 2/2000, Meteorological Synthesizing Centre – East, Moscow, Russia.
- Lindqvist O. and Rodhe H. [1985] Atmospheric mercury - a review. *Tellus* **37B**, 136-157.
- Marchuk G. I. [1974] *Numerical methods in weather prediction*. Academic, New York.
- McRae G. J., Goodin W. R., Seinfeld J. H. [1982] Numerical solution of the atmospheric diffusion equation for chemically reacting flows. *Journal of Computational Physics* **45**, 1-42.
- Nriagu J. O. [1989] A global assessment of natural sources of atmospheric trace metals. *Nature* **338**, 47-49.
- Pacyna J. M., Scholtz M. T., and Li Y.-F. [1995] Global Budgets of Trace Metal Sources, *Environmental Reviews*, **3**, 145-159.
- Ryaboshapko A., Ilyin I., Gusev A., Afinogenova O., Berg T. and Hjellbrekke A.-G. [1999] Monitoring and modelling of lead, cadmium and mercury transboundary transport in the atmosphere of Europe. Joint report of EMEP centres: MSC-E and CCC, EMEP Report 3/99, Meteorological Synthesizing Centre – East, Moscow, Russia.
- Ryaboshapko A., Ilyin I., Bullock R., Ebinghaus R., Lohman K., Munthe J., Petersen G., Segneur C., Wangberg I. [2001] Intercomparison study of numerical models for long-range atmospheric transport of mercury. Stage I: Comparison of chemical modules for mercury transformations in a cloud/fog environment. *EMEP/MSC-E Technical report 2/2001*, Meteorological Synthesizing Centre – East, Moscow, Russia.
- Smolarkiewicz P. K. [1982] The threedimensional Crowley advection scheme. *Monthly Weather Review* **110**, 1968-1983.
- Sofiev M., Maslyaev A., and Gusev A. [1996] Heavy metal model intercomparison. Methodology and results for Pb in 1990. *EMEP/MSC-E Report 2/96*, Meteorological Synthesizing Centre – East, Moscow, Russia.
- Travnikov O. [2000] Uncertainty analysis of heavy metals long-range transport modelling. *EMEP/MSC-E Technical note 9/2000*, Meteorological Synthesizing Centre – East, Moscow, Russia.
- Vulykh N. and Putilina V. [2000] Hexachlorobenzene: Properties, emissions and content in the environment. *EMEP/MSC-E Technical note 6/2000*, Meteorological Synthesizing Centre – East, Moscow, Russia.
- Yanenko N. N. [1971] *The method of fractional steps*. Springer-Verlag, New York.

Mathematics are all well and good but Nature  
keeps dragging us around by the nose

*Albert Einstein*

## Annex A

### Bott advection scheme in spherical co-ordinates

The part of the transport equation (2.5) describing horizontal advection has the following divergent form:

$$\frac{\partial \psi}{\partial t} = -\frac{1}{R_E \cos \varphi} \left[ \frac{\partial (\psi V_\lambda)}{\partial \lambda} + \frac{\partial (\psi V_\varphi \cos \varphi)}{\partial \varphi} \right] \quad (\text{A.1})$$

A sketch and notations of the horizontal grid structure in spherical co-ordinates is depicted in Figure A.1. We shall denote grid cells by whole indexes assuming that scalar values are referred to the centers of a grid cell, while vectors (wind speed and fluxes) are related to the cell faces.

Subscripts  $\lambda$  and  $\varphi$  denote a vector components in zonal and meridional directions respectively.

Superscripts 'e', 'w', 'n', and 's' describe eastern, western, northern, and southern cell faces respectively as well as quantities related to them.

To construct the flux-form numerical scheme we integrate Eq. (A.1) over the grid cell  $(i,j)$ :

$$\int_{S_{ij}} \frac{\partial \psi}{\partial t} ds = - \int_{S_{ij}} \frac{1}{R_E \cos \varphi} \left[ \frac{\partial (\psi V_\lambda)}{\partial \lambda} + \frac{\partial (\psi V_\varphi \cos \varphi)}{\partial \varphi} \right] ds, \quad (\text{A.2})$$

where  $ds = R_E^2 \cos \varphi d\varphi d\lambda$  is the area element, and  $S_{ij} = 2R_E^2 \Delta\lambda \sin \frac{\Delta\varphi}{2} \cos \varphi_j$  is the cell  $(i,j)$  area.

Introducing mass fluxes:

$$F_\lambda = \frac{\psi V_\lambda}{R_E \cos \varphi_j}, \quad F_\varphi = \frac{\psi V_\varphi}{R_E} \cos \varphi \quad (\text{A.3})$$

Eq. (A.2) can be rewritten as follows:

$$\frac{\partial \psi_{ij}}{\partial t} = -\frac{\Delta\varphi (F_\lambda^e - F_\lambda^w)}{2\Delta\lambda \sin \frac{\Delta\varphi}{2}} - \frac{F_\varphi^n - F_\varphi^s}{2 \sin \frac{\Delta\varphi}{2} \cos \varphi_j}. \quad (\text{A.4})$$

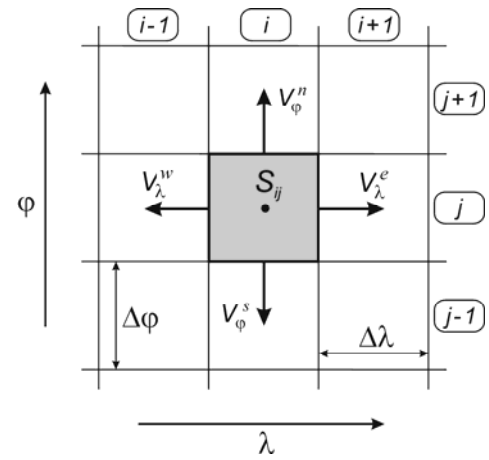


**Figure A.1.** Scheme of the horizontal grid structure in spherical co-ordinates

Here mass fluxes through the appropriate cell faces are:

$$\begin{aligned} F_{\lambda}^e &= \frac{1}{R_E \cos \varphi_j} (\psi_{ij}^e U_{ij}^e - \psi_{i+1j}^w U_{i+1j}^w), & F_{\lambda}^w &= \frac{1}{R_E \cos \varphi_j} (\psi_{i-1j}^e U_{i-1j}^e - \psi_{ij}^w U_{ij}^w), \\ F_{\varphi}^n &= \frac{\cos(\varphi_j + \frac{\Delta\varphi}{2})}{R_E} (\psi_{ij}^n U_{ij}^n - \psi_{ij+1}^s U_{ij+1}^s), & F_{\varphi}^s &= \frac{\cos(\varphi_j - \frac{\Delta\varphi}{2})}{R_E} (\psi_{ij-1}^n U_{ij-1}^n - \psi_{ij}^s U_{ij}^s), \end{aligned} \quad (\text{A.5})$$

and outgoing velocities are defined as  $U_{ij}^{e,n} = \frac{1}{2}(V_{\lambda}^{e,n} + |V_{\lambda}^{e,n}|)_{ij}$  and  $U_{ij}^{w,s} = -\frac{1}{2}(V_{\varphi}^{w,s} - |V_{\varphi}^{w,s}|)_{ij}$ .

Quantities  $\psi_{ij}^{e,w,n,s} = \psi_{ij}^{e,w,n,s}(t)$  describe time depending values of  $\psi$  at the cell  $(i,j)$  faces.

Other components of the mass fluxes are assumed to be constant during a time step.

To obtain expression for the  $\psi_{ij}^{n+1}$  at the time moment  $t_{n+1}$  one should integrate Eq. (A.4) over the time step  $\Delta t$ :

$$\psi_{ij}^{n+1} = \psi_{ij}^n - \frac{\Delta\varphi(M_{\lambda}^e - M_{\lambda}^w)}{2\Delta\lambda \sin \frac{\Delta\varphi}{2}} - \frac{M_{\varphi}^n - M_{\varphi}^s}{2 \sin \frac{\Delta\varphi}{2} \cos \varphi_j}, \quad (\text{A.6})$$

where  $M$  is the mass coming through the unit area of the appropriate cell face during the time step  $\Delta t$ :

$$M_{\lambda}^{e,w} = \int_{t_n}^{t_{n+1}} F_{\lambda}^{e,w} dt, \quad M_{\varphi}^{n,s} = \int_{t_n}^{t_{n+1}} F_{\varphi}^{n,s} dt. \quad (\text{A.7})$$

Expecting subgrid distribution  $\psi_i = \psi_{ij}(\lambda, \varphi)$  inside the cell we can express time depending boundary values of  $\psi$  at the cell faces through the spatial variables:

$$\psi_{ij}^{e,w}(t) = \psi_{ij}(\lambda(t), \varphi_j), \quad \psi_{ij}^{n,s}(t) = \psi_{ij}(\lambda_i, \varphi(t)), \quad (\text{A.8})$$

where time functions  $\lambda(t)$  and  $\varphi(t)$  are defined by the full time derivatives of the coordinates:

$$\frac{d\lambda}{dt} = \frac{V_{\lambda}}{R_E \cos \varphi_j}, \quad \frac{d\varphi}{dt} = \frac{V_{\varphi}}{R_E}. \quad (\text{A.9})$$

Substituting expressions (A.8) to (A.5) and then to (A.7), and transforming the time differential  $dt$  to appropriate spatial differentials using (A.9) one can obtain the following expressions for the outgoing masses:

$$\begin{aligned} M_{\lambda}^e &= \Delta\lambda(I_{ij}^e - I_{i+1j}^w), & M_{\lambda}^w &= \Delta\lambda(I_{i-1j}^e - I_{ij}^w), \\ M_{\varphi}^n &= \Delta\varphi \cos(\varphi_j + \frac{\Delta\varphi}{2})(I_{ij}^n - I_{ij+1}^s), & M_{\varphi}^s &= \Delta\varphi \cos(\varphi_j - \frac{\Delta\varphi}{2})(I_{ij-1}^n - I_{ij}^s), \end{aligned} \quad (\text{A.10})$$

Where:

$$I_{ij}^e = \int_{\frac{1}{2}-\alpha_{ij}^e}^{\frac{1}{2}} \psi_{ij}(\xi) d\xi, \quad I_{ij}^w = \int_{-\frac{1}{2}}^{-\frac{1}{2}+\alpha_{ij}^w} \psi_{ij}(\xi) d\xi, \quad \xi = \frac{\lambda - \lambda_i}{\Delta\lambda}; \quad (\text{A.11})$$

$$I_{ij}^n = \int_{\frac{1}{2}-\beta_{ij}^n}^{\frac{1}{2}} \psi_{ij}(\zeta) d\zeta, \quad I_{ij}^s = \int_{-\frac{1}{2}}^{-\frac{1}{2}+\beta_{ij}^s} \psi_{ij}(\zeta) d\zeta, \quad \zeta = \frac{\varphi - \varphi_j}{\Delta\varphi}. \quad (\text{A.12})$$

Here and further we omit the unchangeable variable in the  $\psi_{ij}(\lambda, \varphi)$  function. The local Courant numbers in zonal and meridional directions are defined as:

$$\alpha_{ij}^{e,w} = \frac{U_{ij}^{e,w} \Delta t}{R_E \Delta\lambda \cos \varphi_j}, \quad \beta_{ij}^{n,s} = \frac{U_{ij}^{n,s} \Delta t}{R_E \Delta\varphi}. \quad (\text{A.13})$$

Substituting expressions for  $M_\lambda^{e,w}$  and  $M_\varphi^{n,s}$  from (A.10) to (A.6) and transforming cosines we obtain the final expression for  $\psi_{ij}^{n+1}$  value at the next time step:

$$\begin{aligned} \psi_{ij}^{n+1} = & \psi_{ij}^n - \frac{\Delta\varphi}{2 \sin \frac{\Delta\varphi}{2}} (I_{ij}^e + I_{ij}^w - I_{i+1j}^w - I_{i-1j}^e) \\ & - \frac{\Delta\varphi}{2} \cot \frac{\Delta\varphi}{2} (I_{ij}^n + I_{ij}^s - I_{ij+1}^s - I_{ij-1}^n) + \mu_j (I_{ij}^n + I_{ij-1}^n - I_{ij}^s - I_{ij+1}^s), \end{aligned} \quad (\text{A.14})$$

where  $\mu_j = \frac{\Delta\varphi}{2} \tan \varphi_j$ . The second term in the right hand side of Equation (A.14) describes the zonal advection, while the two last terms relate to the meridional one. Notice that the second and the third terms are similar to the original Bott scheme [e.g. *Bott*, 1989a, 1993] if step  $\Delta\varphi$  is small enough. Moreover, the last correction term containing  $\mu_j$  is negligible in the low latitudes, and becomes significant next to the pole.

The subgrid distribution of  $\psi$  within the cell  $(i,j)$  is approximated by polynomials of order  $p$  in zonal and meridional direction respectively:

$$\psi_{ij}(\xi) = \sum_{l=0}^p a_{il} \xi^l, \quad \psi_{ij}(\zeta) = \sum_{l=0}^p b_{jl} \zeta^l. \quad (\text{A.15})$$

The coefficients of the polynomials are determined by  $\psi$  values at the neighboring grid cells [see *Bott*, 1989a,b]:

Zonal ( $\varphi = \varphi_j$ )

$$\psi_{kj} S_{kj} = \int_{S_{ij}} \psi_{ij}(\lambda) ds = S_{kj} \int_{k-i-\frac{1}{2}}^{k-i+\frac{1}{2}} \sum_{l=0}^p a_{il} \xi^l d\xi, \quad k = \overline{i, i \pm (p-1)} \quad (\text{A.16})$$

Meridional ( $\lambda = \lambda_i$ )

$$\psi_{ik} S_{ik} = \int_{S_{ij}} \psi_{ij}(\varphi) ds = R_E^2 \Delta\lambda \Delta\varphi \int_{k-j-\frac{1}{2}}^{k-j+\frac{1}{2}} \sum_{l=0}^p b_{jl} \zeta^l \cos(\zeta \Delta\varphi + \varphi_j) d\zeta, \quad k = \overline{j, j \pm (p-1)} \quad (\text{A.17})$$

Solving the systems of linear algebraic equations (A.16) and (A.17) one can obtain polynomial coefficients  $a_{il}$  and  $b_{jl}$ . The coefficients of the second order Bott polynomials ( $p=2$ ) are presented in Table A.1. As seen from the table the zonal coefficients are coincide with those of the original Bott scheme [e.g. *Bott*, 1989b], while the meridional coefficients contain additional terms becoming negligible when  $\mu_j$  tends to zero. Substituting the polynomial coefficients to the expressions (A.15) one can calculate the integrals (A.11) and (A.12). Thus value of  $\psi$  at the next time step is completely determined by the expression (A.14).

The positive definiteness and monotonicity of the scheme are provided by appropriate nonlinear flux limitation in accordance with [*Bott*, 1992; 1993].

**Table A.1.** Coefficients of the second order Bott polynomials ( $p=2$ ) in spherical coordinates (zonal and meridional directions)

<b>Zonal</b>	
$a_{i0}$	$-\frac{1}{24}(\psi_{i+1j} - 26\psi_{ij} + \psi_{i-1j})$
$a_{i1}$	$\frac{1}{2}(\psi_{i+1j} - \psi_{i-1j})$
$a_{i2}$	$\frac{1}{2}(\psi_{i+1j} - 2\psi_{ij} + \psi_{i-1j})$
<b>Meridional</b>	
$b_{j0}$	$-\frac{1}{24}[\psi_{ij+1} - 26\psi_{ij} + \psi_{ij-1} - 2\mu_j(\psi_{j+1} - \psi_{j-1})]$
$b_{j1}$	$\frac{1}{2}[\psi_{ij+1} - \psi_{ij-1} + \frac{\mu_j}{3-7\mu_j^2}(\psi_{ij+1} - 2\psi_{ij} + \psi_{ij-1})]$
$b_{j2}$	$\frac{1}{2}(1 + \frac{2\mu_j^2}{3-7\mu_j^2})(\psi_{ij+1} - 2\psi_{ij} + \psi_{ij-1})$

### **The Pole**

The polar cell of the grid requires separate consideration due to its peculiar geometry. Integrating equation (A.1) over the polar cell with the area  $S_p = 2\pi R_E^2(1 - \cos \frac{\Delta\phi}{2})$  one can obtain:

$$\frac{\partial \psi}{\partial t} = \frac{1}{N_\lambda(1 - \cos \frac{\Delta\phi}{2})} \sum_{i=1}^{N_\lambda} F_{iP}^s, \quad (\text{A.18})$$

where  $N_\lambda = 2\pi/\Delta\lambda$  is the number of cells in zonal directions; capital  $P$  denotes quantities related to the polar cell. Meridional mass fluxes through the polar cell faces are:

$$F_{iP}^s = \frac{\sin \frac{\Delta\varphi}{2}}{R_E} (\psi_P U_{iP}^n - \psi_{iP-1} U_{iP-1}^s), \quad i = \overline{1, N_\lambda} \quad (\text{A.19})$$

Following the procedure presented above we derive expression for  $\psi$  value at the next time step:

$$\psi_P^{n+1} = \psi_P^n + \frac{\Delta\varphi \cot \frac{\Delta\varphi}{4}}{N_\lambda} \sum_{i=1}^{N_\lambda} (I_{iP-1}^n - I_{iP}^s) \quad (\text{A.20})$$

The distribution within the polar cell is approximated by a piecewise continuous surface consisting of  $N_\lambda / 2$  polynomial-shaped sectors divided by meridians and converging to the pole point

$$\psi_i^P(\zeta) = \sum_{l=0}^p b_{il}^P \zeta^l, \quad i = \overline{1, N_\lambda / 2}$$

Solving the system of algebraic equations similar to (A.16) one can obtain polynomial coefficients for the polar cell. The coefficients of second order Bott polynomials ( $p=2$ ) for the polar cell are presented in Table A.2. Integral terms in equation (A.20) corresponding to outgoing fluxes are calculated as follows:

$$I_{iP}^s = \begin{cases} \int_{-\frac{1}{2} + \beta_{iP}^s}^{-\frac{1}{2}} \psi_i^P(\zeta) d\zeta, & i = \overline{1, \frac{N_\lambda}{2}} \\ \int_{\frac{1}{2} - \beta_{iP}^s}^{\frac{1}{2}} \psi_{i - \frac{N_\lambda}{2}}^P(\zeta) d\zeta, & i = \overline{\frac{N_\lambda}{2} + 1, N_\lambda} \end{cases} \quad (\text{A.21})$$

The terms related to the incoming fluxes  $I_{iP-1}^n$  are computed according to (A.12).

**Table A.2.** Coefficients of the second order Bott polynomials ( $p=2$ ) for the polar cell

Polar	
$b_{i0}^P$	$\frac{10}{9} \psi_P - \frac{1}{9N_\lambda} \sum_{i=1}^{\frac{N_\lambda}{2}} (\psi_{iP-1} + \psi_{i+\frac{N_\lambda}{2}P-1})$
$b_{i1}^P$	$\frac{6}{13} (\psi_{i+\frac{N_\lambda}{2}P-1} - \psi_{iP-1})$
$b_{i2}^P$	$-\frac{8}{9} \psi_P + \frac{2}{5} (\psi_{iP-1} + \psi_{i+\frac{N_\lambda}{2}P-1}) + \frac{4}{45N_\lambda} \sum_{i=1}^{\frac{N_\lambda}{2}} (\psi_{iP-1} + \psi_{i+\frac{N_\lambda}{2}P-1})$